**Crystal habits of itraconazole microcrystals: unusual isomorphic intergrowths induced via tuning recrystallisation conditions**

Naila A. Mugheirbi and Lidia Tajber*

School of Pharmacy and Pharmaceutical Sciences, Trinity College Dublin, Dublin 2, Ireland.

* to whom correspondence should be addressed: lidia.tajber@tcd.ie, Phone: 00353 1 896 2787 Fax: 00353 1 896 2810

**Abstract**

The external appearance of a crystal of active pharmaceutical ingredient (API), usually referred to as a crystal habit, has a substantial impact on the API's physicochemical and physiochemical properties and, subsequently, its pharmaceutical performance. In this work, we investigate the role of different parameters of antisolvent crystallisation impacting on the itraconazole (ITR) crystal habit and how this crystal habit manipulation, including crystal intergrowth, can affect crystal interactions with water molecules. Three distinct isomorphic crystal habits of ITR, a twinned blade-shaped ($CH_{tw}$), a plate-shaped ($CH_{pl}$) and a flat sheet-shaped with dendritic ends ($CH_{sh}$) were obtained by controlling crystallisation conditions. A liquid-liquid crystalline phase separation was observed as an intermediate stage preceding crystal growth. The March-Dollase parameter was used as a quantitative description of the preferred orientation, where $CH_{sh}$ exhibited the highest preferred orientation. The three crystal habits were evaluated for their wettability and water vapour distribution, at 37 °C, using the Young-Nelson fitting model. $CH_{tw}$ crystals sorbed a statistically significantly higher amount of water than $CH_{pl}$ and $CH_{sh}$, which was attributed to the presence of crystal defects due to the twinning boundary. On the other hand, the amount of water adsorbed on the surface of $CH_{pl}$ and $CH_{sh}$ crystals was comparable and it was about twice that adsorbed on $CH_{tw}$ crystals. This was related to the abundance of hydrophilic chemical functionalities on the (010) facet of $CH_{pl}$ and $CH_{sh}$ as supported by the full interaction map carried out using Mercury software. This study expands investigations of the impact of crystal habit manipulation on API's functional properties beyond the well-known solubility improvement approaches.

Keywords: Itraconazole, Crystal habit, Liquid-liquid crystalline phase separation, Antisolvent crystallisation, Preferred orientation.

## 1. Introduction

Solid active pharmaceutical ingredients (APIs) are usually synthesized via crystallisation from solution [1]. Crystallisation is usually achieved by creating supersaturated conditions, with respect to the API, via cooling a hot solution, antisolvent precipitation or slow evaporation [2, 3]. Crystalline materials exhibit a higher thermodynamic stability than their amorphous counterparts, thus encounter less difficulties during e.g. a pharmaceutical manufacturing process [4]. Many drugs can exist in more than one polymorphic form, where the space-lattice arrangement of molecules is distinctive in each crystal form depending on the crystallisation conditions used, such as the solvent nature, cooling and/or mixing rate, pressure and the inclusion of a co-solvent and other solutes [5, 6]. Crystalline materials can also be rendered in different crystal habits where the growth of one or more crystal faces is promoted or inhibited [7].

In general, the area of pharmaceutical performance design via polymorphic manipulation is more extensively studied compared to crystal habit manipulation, although the latter has a surmised influence on the behaviour of the final product including tablettability, wettability and dissolution properties [8, 9]. Recently, it has been demonstrated for celecoxib that the crystal habit of this compound has a considerable impact on its intrinsic dissolution [10]. While some reports on manipulating crystal habits are available for APIs, the investigation of regular isomorphic intergrowth of crystals remained primarily limited to inorganic materials [11]. A regular intergrowth relation can occur between the same crystal species, which is usually identified as twinning or a parallel intergrowth. It can also be observed between crystals of different species and is referred to as an epitaxial growth. Twinning is an intergrowth between two crystals of the same species by a symmetry operation, which is not part of the single crystal. Twinning can occur during the process of crystallisation, transformation and deformation and is referred to as growth twinning, transformation twinning and deformation twinning, respectively [12]. Parallel intergrowth is different from twinning and usually adapted to reduce system energy. It occurs when two or more crystals of the same material are joined in a parallel arrangement with clearly visible parallel extinction [13]. Epitaxy describes the growth of a guest crystal with a certain orientation over a host crystal of different species [12]. A different type of intergrowth is observed for some APIs including aspirin, promethazine and felodipine and referred to as intergrowth polymorphism, in which the single crystal contains distinct domains of different polymorphs [14, 15].

The presence of impurities, additives and other solvents, even at minute quantities, impact the crystallisation process via altering the nucleation and growth rates and thus predetermine the resultant crystal polymorphic forms and/or their crystal habits [16, 17]. Additives can be “tailor-made”, structurally related to the drug with the ability to incorporate into the crystal lattice [18], or polymeric

and surfactant additives with little or no structural similarity to the drug of interest and capable of selective adsorption at the crystal/solution interface [19]. The ultimate crystal shape is governed by the growth kinetic of interfaces to allow maximum growth rate at a given degree of supersaturation that could be due to supercooling [20]. Interrelations occurring between the solute and additives, at the molecular level, that could have kinetic, thermodynamic and molecular recognition origin, remain one of the not fully explored areas of chemistry and physics [16].

Itraconazole (ITR) is a Biopharmaceutics Classification System (BCS) class II triazole antifungal drug [21]. Two crystalline forms have been reported in the scientific literature to date [22, 23] however, to the best of our knowledge, no crystal habit manipulation reports are available in the literature. Crystalline ITR has very low aqueous solubility [24] and could benefit from modifying crystal habit and/or introducing crystal intergrowth. The former can increase the surface area of hydrophilic crystal facets, while the latter can introduce some crystal defects which could increase water penetrability. Herein, we report on three different crystal habits (shapes) of ITR, each having different wettability and moisture sorption properties, thus exhibiting different functional properties relevant to the performance of pharmaceutical drug substances. This study expands the area of crystal habit manipulation beyond the classical simple morphology manipulation to the intricate crystal intergrowth behaviour of a pharmaceutical API and the subsequent impact on its water sorption behaviour. Water sorption properties of a crystalline API are of a great importance since this parameter has been reported to induce caking of powder and can adversely affect drug dissolution rate [25]. In addition, moisture sorption can be correlated with the dissolution rate, as demonstrated recently by Puncochova and co-workers [26]. Twinning and dendritic intergrowth were observed in this study for ITR crystals produced by manipulating antisolvent crystallisation conditions. The recrystallisation process was investigated by monitoring ITR concentration, temperature as well as the shape and the phase of matter of intermediates throughout the process. The effect of the crystallisation conditions on the March-Dollase (MD) parameter, an indication of the preferred orientation and the crystal shape, was investigated. Finally, to complete the studies, computational investigation into the functionalities available on the facets of interest was performed using Mercury 3.5.1 software.

## 2. Experimental and computational methods

### 2.1. Materials

Itraconazole (ITR) was a gift from Neuland Laboratories Ltd. (Welding, Hamburg, Germany). Poloxamer 407 (P407) was purchased from BASF Corp. (Ludwigshafen, Germany). Acetone Chromasolv®, HPLC grade, was purchased from Sigma-Aldrich (Dorset, UK), while acetonitrile HPLC grade was obtained from Fisher Scientific (Loughborough, UK). All other chemicals were analytical grade and used as received.

### 2.2. Antisolvent crystallisation of ITR

The solvent phase was 7.9 mg/ml ITR in acetone (aprotic solvent) at 50 °C (87% of the saturation solubility of ITR in acetone [24]) with or without P407 (at a concentration of 1 mg/ml unless stated otherwise). An aliquot of this solvent phase was rapidly poured into the static thermostated antisolvent phase kept at 0.5, 50 or 80 °C (deionised water, protic solvent) using the following solvent to antisolvent ratios: 2:1, 1:2, 1:2.5 and 1:1 v/v. Conditions associated with the most unique crystal morphologies are displayed in Table 1. To ensure reproducibility, at least four replicates were performed. The formed crystals were centrifuged at 12,000 rpm (4 °C) for 20 min using an Eppendorf 5810R centrifuge (Hamburg, Germany). The supernatant was removed and the solid residue was thoroughly washed using deionised water and dried under nitrogen purge.

**Table 1. Summary of crystallisation conditions associated with the most unique morphology types of ITR crystals.**

| Morphology type** | Antisolvent temperature (°C) | Solvent (S) | Antisolvent (AS) | S:AS (v/v) ratio |
|---|---|---|---|---|
| $CH_{tw}$ | 0.5 | ITR (7.9 mg/ml) and P407 (1 mg/ml) | Deionised water | 2:1 |
| $CH_{Pl}$ | 50 | ITR (7.9 mg/ml) and P407 (1 mg/ml) | Deionised water | 1:2 |
| $CH_{sh}$ | 80 | ITR (7.9 mg/ml) and P407 (8 mg/ml)* | Deionised water | 1:1 |

* The only case where 8 mg/ml P407 was used.
** The abbreviations are described in Section 3.1 and Figure 1.

### 2.3. Characterisation of ITR crystals

#### 2.3.1. Particle size and morphology

A Zeiss Supra variable Pressure Field Emission Scanning Electron Microscope (Germany) equipped with a secondary electron detector and accelerating voltage of 5 kV was used for the morphological examination of ITR crystals and process intermediates. The dried samples were sputter coated with a layer of gold/palladium under vacuum before analysis.

#### 2.3.2. Powder X-ray diffraction

Reflection powder X-ray diffraction (PRXRD) measurements were performed using a Rigaku Miniflex II, a desktop X-ray diffractometer (Japan) operating in the Bragg-Brentano reflection mode, equipped with a Cu Kα radiation X-ray source. The samples were front-loaded on a zero-background silicon sample holder without grinding, gently pressed using a glass slide and scanned over a 2θ range of 2-40°. The texture of the produced crystals was evaluated using the March-Dollase approach to quantitatively describe the preferred orientation. The calculations were performed for samples produced according to the method presented in Section 2.2 using 0.5 to 80 °C antisolvent crystallisation temperature as well as the solvent composition ranging from 28% acetone (equivalent to a 1:2.5 v/v solvent:antisolvent ratio) to 66% acetone (equivalent to a 2:1 v/v solvent:antisolvent ratio) in the final media with and without the inclusion of 1 mg/ml P407 in the solvent phase. The sample $CH_{sh}$ made by applying the conditions outlined in Table 1 was also analysed. The March-Dollase parameter (MD) was calculated using Eq. 1, as described by Zolotoyabko [27].

$$MD = \left[\frac{sin^2\ \alpha}{(k/k_p)^{2/3} - cos^2\ \alpha}\right]^{1/3} \quad \text{Eq. 1}$$

where α is the angle between two reciprocal lattice vectors H and h. H (*HKL*) is the preferably oriented plane and h (*hkl*) corresponds to an atomic plane, inclined by a small angle ($\cos \alpha \leq 1$) with respect to the plane H, with strongly suppressed diffraction peaks. $k$ and $k_p$ are the diffraction intensity ratios for the powder in question and a randomly oriented powder, respectively.

Transmission powder X-ray diffraction (PTXRD) experiments were carried out at room temperature using a Rigaku-Denki D/MAX RAPID II-R diffractometer (Rigaku Corporation, Japan) with a rotating anode Ag Kα tube (λ = 0.5608 Å), an incident beam (002) graphite monochromator and an image plate in the Debye–Scherrer geometry as a detector. The pixel size was 100 µm × 100 µm. All samples were placed inside glass capillaries (1.5 mm in diameter). The measurements were performed for the filled and empty capillaries and then the signal intensity of the empty capillary was subtracted. The beam width at the sample was 0.3 mm. The two-dimensional diffraction patterns were then converted into one-dimensional intensity data by integration around each ring using suitable software [28].

#### 2.3.3. Computational investigations

Powder patterns simulation and interaction maps were generated using Mercury 3.5.1® software (CSD refcode TEHZIP). The surface interaction maps were built using the Superstar approach [29]. Molecules on the surface of interest were split into IsoStar central groups and appropriate 3D scatterplots were then superimposed on the molecules of interest followed by removal of any clashing data points. Normalised density maps were then generated and overlapping maps from the same probe were combined by multiplication followed by the generation of the final interaction map

[30]. Herein, carbonyl, uncharged NH and aromatic CH were employed to probe the interaction maps indicative of H-bond acceptor, H-bond donors and hydrophobic interactions, respectively. Mercury 3.5.1 was also utilised to visualise the accessible voids in a perfectly packed ITR crystal. Hirshfeld surface analysis was performed using CrystalExplorer (ver. 3.0) software [31].

#### 2.3.4. Single crystal X-ray diffraction (SCXRD)

SCXRD was performed to verify the solid-state isomorphic form and to face-index the crystals. A specimen of $CH_{tw}$, approximate dimensions 0.020 mm x 0.040 mm x 0.100 mm, was used for the X-ray crystallographic analysis. The X-ray intensity data were measured at 100(2)K using a Bruker Apex Duo system equipped with an Oxford Cryosystems Cobra low temperature device and using a MiTeGen micromount. Bruker APEX2 software was used to correct for Lorentz and polarization effects. A total of 2743 frames were collected. The total exposure time was 42.67 hours. The frames were integrated with the Bruker SAINT software package using a narrow-frame algorithm. This analysis was carried out in triplicate on separate crystals.

#### 2.3.5. Differential scanning calorimetry (DSC)

Accurately weighed samples (3-5 mg) were placed in pin-holed aluminium pans. The DSC measurements were performed using a Mettler Toledo DSC 821e (Greifensee, Switzerland) and a nitrogen purge at a speed of 10 ml/min. A temperature range of 25-200 °C was applied with a heating rate of 10 °C/min.

#### 2.3.6. Optical and polarized light microscopy

Optical and polarized light (PL) microscopy was performed with an Olympus BX53 polarizing optical microscope equipped with a U-POT cross polarizer and a Q IMAGING Fast 1394 camera. Samples were either dried before analysis or analysed in the crystallisation medium.

### 2.4. Crystal formation monitoring

#### 2.4.1. Change in ITR concentration in the crystallisation media

The change in the concentration of ITR in the solution upon the addition of the solvent phase to the antisolvent phase and throughout the crystallisation process was monitored. For each preparation condition, as summarised in Table 1, an aliquot was withdrawn at predetermined time points (0, 2, 5, 10, 20 and 40 min) following the addition of the solvent phase to the antisolvent phase. The aliquot was filtered using 0.1 µm PTFE filter membrane (Whatman, UK), diluted with the mobile phase and ITR concentration was determined using a HPLC method as described before[24]. The net temperature of the crystallisation media was measured simultaneously.

#### 2.4.2. Morphology of crystallisation process intermediates

The morphology of the intermediate phases was characterised using SEM and TEM as described above. For SEM, aliquots of the various liquids were placed directly on silicon chips 5*7 mm with

(111) orientation fixed on aluminium stubs and then dried using nitrogen purge. Transmission electron microscopy (TEM) characterisation of the crystallisation process intermediates was carried out on a TEM Titan instrument (FEI Ltd, Hillsboro, OR, USA). An aliquot of the crystallisation solution was drop casted on Cu holey carbon-coated TEM grids and imaged at 300 kV.

### 2.5. Contact angle measurement

Sessile drop contact angle can be measured on the surface of compressed disc or on a layer of powder adhered to an inert substrate [32, 33]. The former is the most widely used and the latter are used to avoid unintended crystal structure modification upon compaction. Here, the thin layer method was adopted with some changes. A thin powder film prepared immediately following crystallisation was used where the crystals were filtered under vacuum for 20 seconds. The produced film was then washed with deionised water under vacuum filtration for 1 min and carefully transferred to a glass slide and left to dry overnight. Advancing contact angle of double distilled water drops with the prepared films were calculated at ambient conditions using a Drop Shape analyser (FTA 125, First Ten Angstrom, Virginia, USA). From the captured photos, the contact angle was calculated based on the Young-Laplace equation [34]. The slope of the tangent to the drop at the liquid−solid−vapour interface line was calculated. All measurements were performed in triplicate under ambient conditions of 25±2 °C.

### 2.6. Dynamic vapour sorption and mathematical modelling of moisture distribution

Moisture absorption/adsorption behaviour characteristic of each sample was monitored using a DVS advantage-1 automated gravimetric vapour sorption analyser (Surface Measurement Systems Ltd., London, UK). Samples were equilibrated at 0% RH until dry (d$m$/dt ≤ 0.002 mg/min for at least 10 min) and the reference mass was recorded. Each sample was exposed to a relative humidity profile from 0% to 90% and back to 0% RH with 10% steps at 37 ± 0.1 °C.

The Young-Nelson model was fitted to the sorption-desorption isotherms. The model can differentiate between bound monolayer, externally adsorbed multilayer and internally absorbed water using the following equations [35];

$$M_s = A(\beta + \theta) + B\theta\mathrm{RH} \quad \text{Eq. 2}$$

$$M_d = A(\beta + \theta) + B\theta\mathrm{RH}_{max} \quad \text{Eq. 3}$$

Where $M_s$ and $M_d$ are the mass percentage of water sorbed and desorbed on the crystals at each %RH equilibrium. A and B are constants characteristic of each system. In the used model, $\theta$ is the fraction of the surface covered by at least one layer of water molecules and $A\theta$ is the mass of water in a complete adsorbed monolayer expressed as a fraction of the dry mass of the crystals. $A(\beta + \theta)$ is the total amount of adsorbed water and $A\beta$ is the mass of water which is adsorbed as a

multilayer. B is the mass of absorbed water at 100% RH, thus $B\theta\mathrm{RH}$ is the mass of the absorbed water when the monolayer coverage is $\theta$ and the relative humidity is RH.

$\theta$ and $\beta$ can be expressed mathematically as:

$$\theta = \frac{RH}{RH + E(1-RH)} \quad \text{Eq. 4}$$

$$\beta = -\frac{ERH}{E-(E-1)RH} + \frac{E^2}{(E-1)}\ln\left[\frac{E-(E-1)RH}{E}\right] - (E+1)\ln(1-RH) \quad \text{Eq. 5}$$

Where E is equilibrium constant between monolayer water and the 'normally condensed' water adsorbed externally to the monolayer and is depending on the material. All data were fitted to Eq. 2 and 3 using multiple linear regression and the sum of squares of the residuals between the experimental and the calculated values were used as the fitting criteria. The corresponding profiles of water adsorbed in monolayer ($A\theta$), multilayer ($A\beta$) and absorbed ($B\theta\mathrm{RH}$) were constructed from the estimated values of A, B and E using the above equations.

### 2.7. Statistical analysis

Statistical analyses were performed via one way ANOVA with the Tukey comparison test using Minitab Release 16. For all tests, $p \leq 0.05$ was used as the criterion to assess statistical significance.

## 3. Results and discussion

### 3.1. Crystal morphology

Crystallisation of ITR was achieved via tuning the antisolvent crystallisation conditions by controlling the percentage of the added solvent in the final volume (expressed as a solvent to antisolvent ratio), cooling temperature, polymer concentration and precipitation temperature (antisolvent temperature). Preparative conditions associated with the most characteristic shape types (habits) are summarised in Table 1. SE micrographs and polarized light (PL) microscope images (Figure 1) revealed a twining behaviour of ITR crystals ($CH_{tw}$), with a characteristic blade like shape of the principal (parent) crystals. Multiple or repeated twinning dominates the sample, where several daughter crystals are arranged in a radiating pattern as an example of interpenetration growth twinning. A different type of intergrowth was observed in the $CH_{sh}$ sample, where each crystal is visible as a very thin, brittle sheet with branched ends. A similar plagioclase crystal shape was described as a tabular crystal with dendritic projections from the corners [36]. Thus, $CH_{sh}$ crystals can be described as sheets with dendritic ends since they are too thin to be tabular.[12]. The third crystal habit was a thin-plate like morphology ($CH_{pl}$) under the optical microscope and confirmed by SEM (Figure 1c). Birefringence was observed for all crystal habits under cross polarized light microscope (PLM), indicating their crystalline nature. Sloped ends were observed for $CH_{tw}$ and $CH_{pl}$ in SE micrographs and confirmed by PLM.

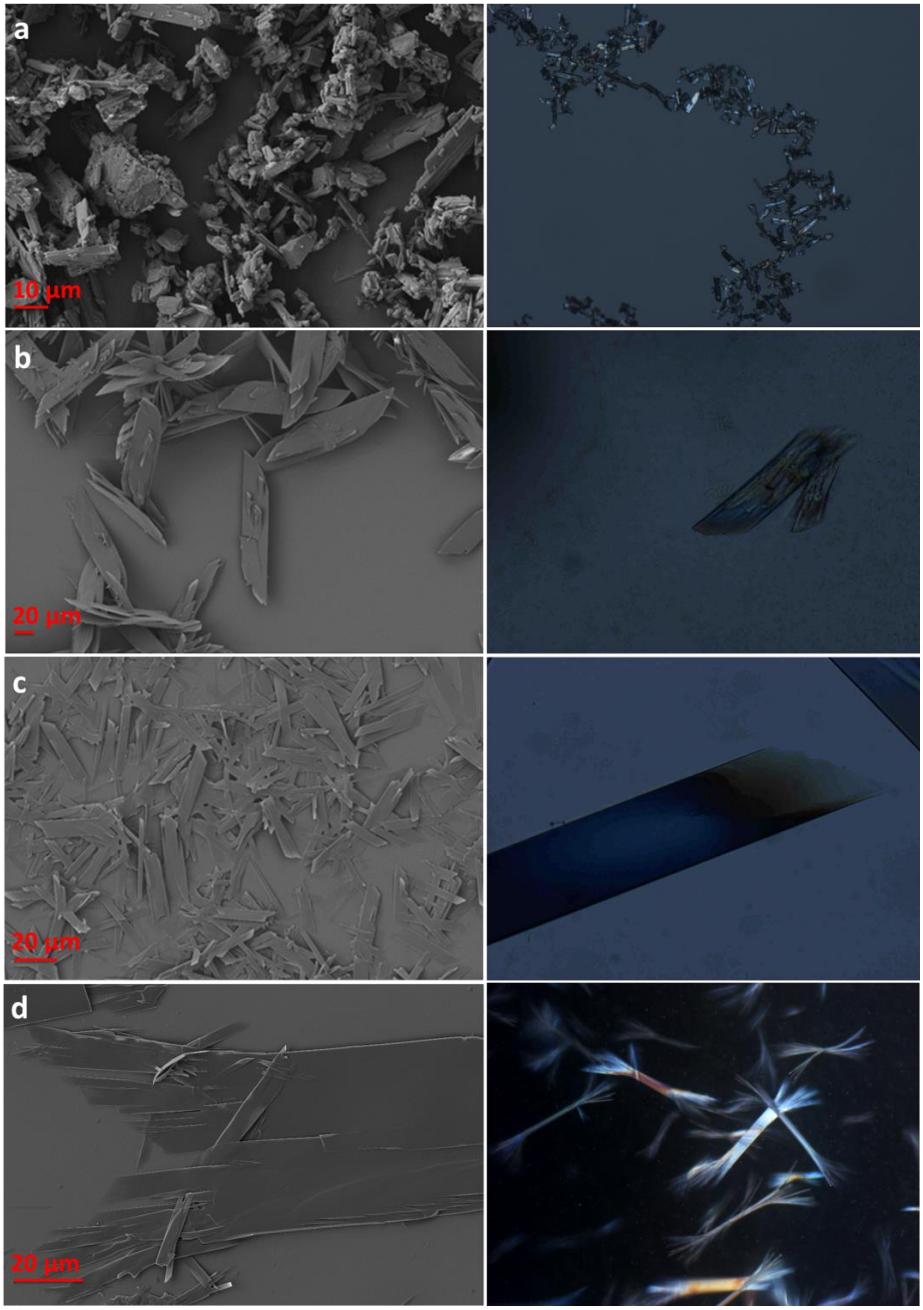


**Figure 1. SE micrographs (left) and PL images (right) of: (a) as-received ITR, (b) $CH_{tw}$, (c) $CH_{Pl}$ and (d) $CH_{sh}$. All PL imaging was performed on dried crystals except for $CH_{sh}$, where the crystals were imaged in the crystallisation solution to avoid breakage of the characteristic dendritic ends.**

### 3.2. Powder X-ray diffraction

PRXRD diffractograms (Figure 2) confirmed the crystalline nature of all samples. Remarkable variations in relative intensities of some peaks were observed. To rule out any possible polymorphic crystallisation, PRXRD patterns of all crystallised forms were compared with the simulated powder pattern, generated using Mercury 3.5.1 software (Figure SI.1), with the assumption of a random crystal orientation, which revealed that all habits had superimposable peaks with the simulated

pattern (CSD refcode TEHZIP). Moreover, one dimensional and two dimensional PTXRD patterns (Figure SI.2) were identical for the three samples further confirming the isomorphic phase of the ITR crystals. PTXRD also indicates that this type of twinning observed in $CH_{tw}$ is simple contact twinning because the daughter crystals did not introduce any diffraction complications to the diffraction patterns [37].

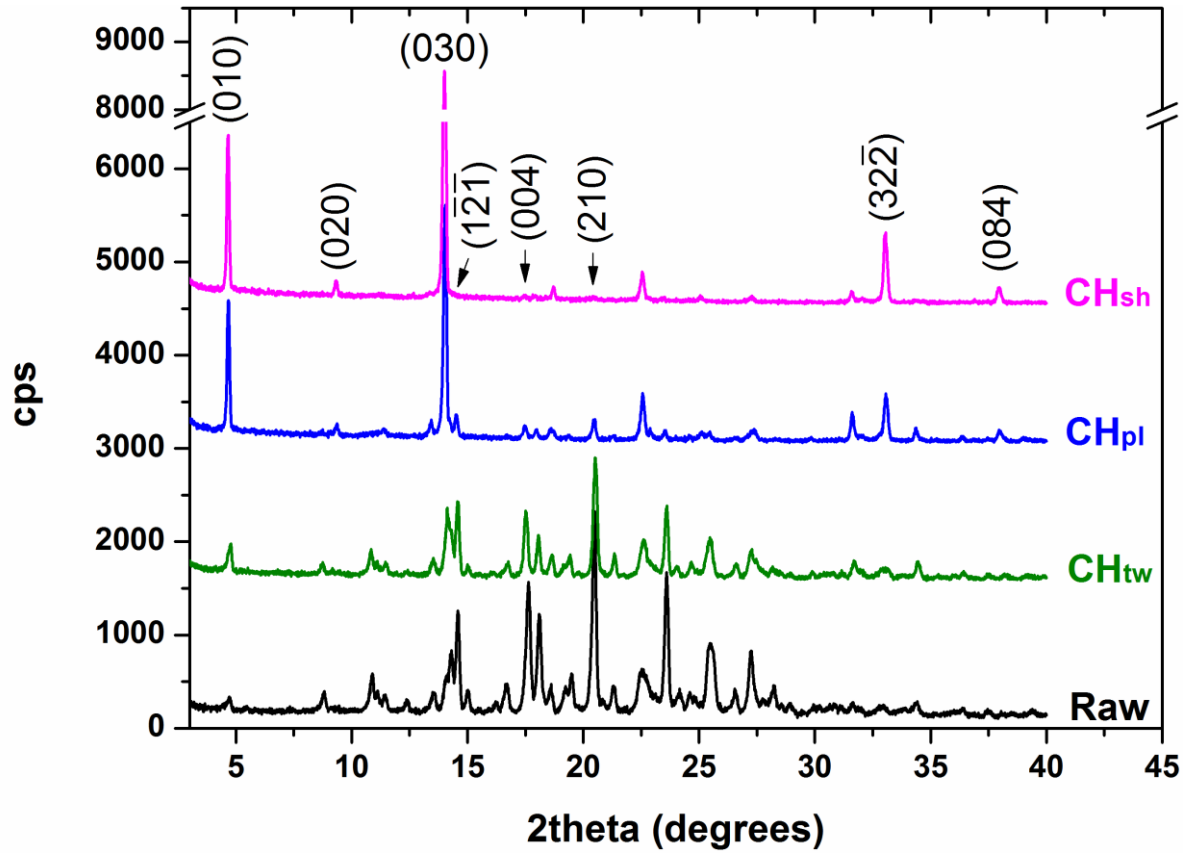


**Figure 2. Overlay of PRXRD diffractograms of the three principal crystal habits ($CH_{tw}$, $CH_{pl}$ and $CH_{sh}$) and the starting material (Raw). The Miller indices (hkl) of the affected facets/planes are labelled.**

Preferred orientation was utilised to assign the large crystal facets/planes. For $CH_{tw}$, an increase, in comparison to the starting material, in the intensity of the diffraction peak corresponding to the (030) was observed. For $CH_{pl}$ and $CH_{sh}$, the plane (030) was associated with the highest intensity indicating an enhanced diffraction originating from the (0$l$0) reflections. It should be highlighted that the intensity of the peak at 17.5 2θ°, corresponding to the atomic plane (004), was reduced in all samples. Therefore, (030) and (004) were chosen as the lattice vectors H and h, respectively, to calculate the March-Dollase parameter (MD). The calculations were performed for samples manufactured using a range of recrystallisation conditions, as described in Sections 2.2 and 2.3.2, including the three principal and characteristic crystal habits (conditions of the preparative process are presented in Table 1). Results are plotted as contour maps, separate for samples crystallised with

and without P407 along with the simulated powder patterns in Figure 3. The MD parameter ($0 \leq MD \leq 1$) is an indication of the degree of the preferred orientation of the sample on the sample holder, which in turn is related to the crystal shape. A value of 0 is an indication of absolute preferred orientation, which is usually observed with flat anisotropic crystals, while a value of 1 is an indication of randomly oriented powder (zero preferred orientation) and indicates isotropic crystal shapes [38]. The white regions in the plot (Figure 3) represent the conditions where a non-crystalline product was obtained and their location appears to be identical in the absence and presence of P407. The black regions, corresponding to the MD parameter below 0.4, was absent in the maps indicating that the $CH_{sh}$ habit can only be obtained using 8 mg/ml P407 and cannot be obtained using any other of the investigated combination of conditions using 1 mg/ml P407 in acetone or just acetone. The $CH_{pl}$ habit with the MD parameter less than 0.5 (dark blue regions) can only be obtained when a low solvent/antisolvent ratio is used with the antisolvent temperature above 45 °C and in the presence of P407. The cyan and green regions, with the MD parameters between 0.5 and 0.8, correspond to the conditions where twinning (habit $CH_{tw}$) is expected to take place. The polymer appears to be inducing twinning at high antisolvent temperatures and high solvent contents, however the same combinations of conditions (antisolvent temperature and solvent content) when no P407 was used resulted in almost isotropic crystals with the MD parameter ≥ 0.8. P407 has surfactant properties which have been reported to trigger twinning [11]. It is worth mentioning that the PRXRD pattern of ITR as supplied (raw material, Figure 2) was similar to the simulated powder patterns when the MD parameter is around 0.9, indicating that the starting material was not a fully isotropic powder, confirmed by the SE micrograph (Figure 1a), as some anisotropic crystals can be observed in the specimen. Moreover, the contour maps revealed that, in order to obtain fully isotropic faceted crystals, the solvent and antisolvent should be mixed in comparable volumes and the antisolvent temperature should be below 20 °C, in case where no polymer is added to the crystallisation mix, and below 10 °C, if P407 is included in the solvent phase.

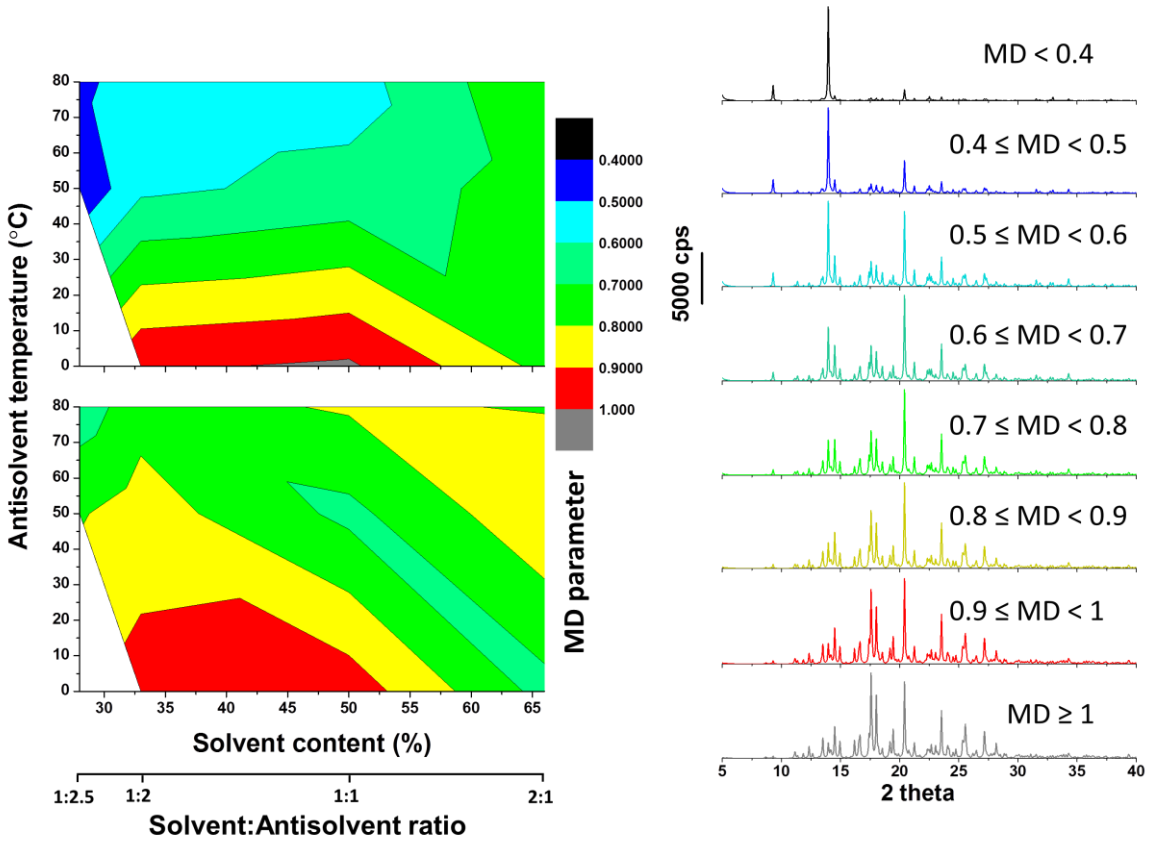


**Figure 3. Contour maps (antisolvent temperature versus solvent content) of the MD parameter values for the crystallised ITR samples along with the calculated powder X-ray diffraction patterns for the different MD values. Upper map: data pertaining to the samples containing 1 mg/ml P407 in the solvent phase (1 mg/ml P407 in acetone) and lower map: data pertaining to the samples containing no polymer in the solvent phase (ITR in pure acetone).**

### 3.3. Thermal analysis

The DSC investigation demonstrated subtle differences in the melting temperature of the different crystal habits (Figure SI.3). $CH_{sh}$ exhibited the lowest melting point (162.9 °C, peak value 165.7 °C) among the crystalline samples, compared to the melting point of 166.1 °C of the starting material powder and $CH_{tw}$. The melting point appearing at a lower temperature could be attributed to the dendritic intergrowth in $CH_{sh}$, where the small protruding ends readily break to form fines. Subtle changes in melting points upon changing the crystal habit have been reported before for nifedipine and were attributed to the difference in in the examined habits' crystal size [39]. Grinding pretreatment was avoided in our study to prevent unintended phase changes.

### 3.4. Crystal formation process and intermediates investigation

Data pertaining to monitoring the crystallisation process kinetics resulting in the principal ITR crystal habits is displayed in Figure 4. During crystallisation of $CH_{tw}$ a cloudy dispersion formed initially upon addition of the solvent phase to the antisolvent phase and nearly instantly disappeared ($CH_{tw}$ images 1 and 2 in Figure SI.4). Monitoring the concentration of ITR in solution supports the visual observation as a spike in soluble ITR at around 2 minutes, net temperature 6.9±0.2 °C, indicates solubilisation of the initially formed cloudy dispersion. As the solution cooled further to 1.7±0.2 °C, ITR concentration in the solution continued to decrease indicating an initiation of the crystallisation process as shown in Figure 4 ($CH_{tw}$ image 3 in Figure SI.4).

In contrast, crystallisation of $CH_{pl}$ and $CH_{sh}$ followed a different kinetics. Both crystallisation mixtures became cloudy upon the addition of the solvent to the antisolvent phase ($CH_{pl}$ and $CH_{sh}$ image 1 in Figure SI.4) and remained so until shiny crystals began to be noticeable ($CH_{pl}$ and $CH_{sh}$ image 2 in Figure SI.4). Throughout the sampling period, ITR available in the solution decreased gradually with similar concentration profiles for both $CH_{pl}$ and $CH_{sh}$ over the first 20 minutes of the crystallisation process. Temperature profiles were different with 14.3 and 28.2 °C fall in the temperature of the media for $CH_{pl}$ and $CH_{sh}$, respectively, after first 2 minutes. For the next 3 minutes, the temperatures further decreased by 5.45 and 12.85 °C for the $CH_{pl}$ and $CH_{sh}$ crystallisation media, respectively. For the following 20 minutes, a higher decrease in ITR concentration in solution was observed for $CH_{sh}$ compared to $CH_{pl}$, while the temperature drop was comparable for both systems.

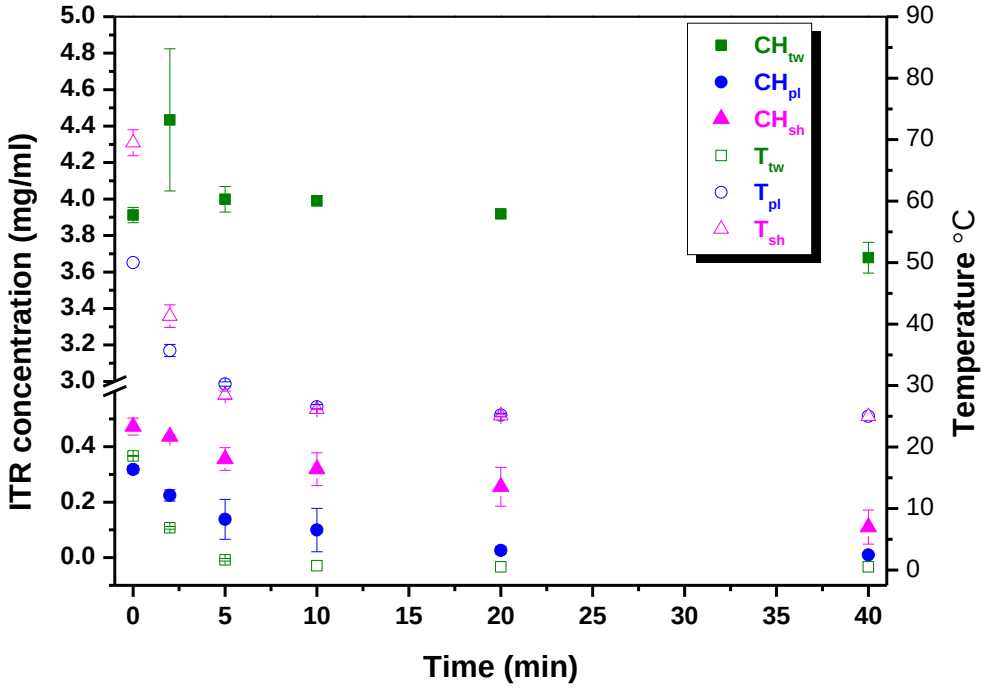


**Figure 4. Concentration versus time (closed symbols) and temperature versus time (open symbols) profiles for the crystallisation processes of the principal crystal forms of ITR.**

The various stages of the crystallisation process can be interpreted using morphologies of the intermediate products observed by SEM, PLM and TEM (Figure 5). For $CH_{pl}$ and $CH_{sh,}$, as the solvent was added to the antisolvent, spherical particles with a wide size range (300 nm to 4 μm) were formed (1st intermediate) as shown in Figure 5a, b and d. Those particles were liquid crystalline (LC) as concluded from their birefringent nature with Maltese crosses signifying the LC formation [40] (Figure 5d). The LC phase of ITR has been reported to possess higher solubility than the crystalline phase [24]. These particles underwent Ostwald ripening and, due to availability of soluble ITR, this phase transformed as explicitly presented by the particles representing steps 1, 2 and 3 in Figure 5a and Figure 5c. Those square shaped structures (2nd intermediate) continued to grow for the rest of the crystallisation process and coexisted with the final crystals when the crystallisation liquor was sampled later (Figure SI.5).

In contrast, for the $CH_{tw}$, the LC intermediate formation was anticipated, however it could not be isolated as this phase readily solubilised due to the presence of a high content of acetone (solvent), which explains visually clearing the solution after two minutes from the mixing and the high concentration of soluble ITR detected in the crystallisation mix (Figure 4 and Figure SI.4 $CH_{tw}$ image 2). As the cooling process proceed nucleation and subsequent crystallisation continued. ITR was recently reported, by our group, to form stable liquid crystalline nanoparticles (LC NPs), in nematic as well as smectic phases, using a 1:10 v/v acetone:water system [41]. It should be highlighted that a liquid-liquid phase separation [42] and liquid-glass phase separation [43] have been reported before as intermediate stages occurring before crystallisation and herein we observe a new phenomenon of a liquid-liquid crystal phase separation preceding crystallisation of an API.

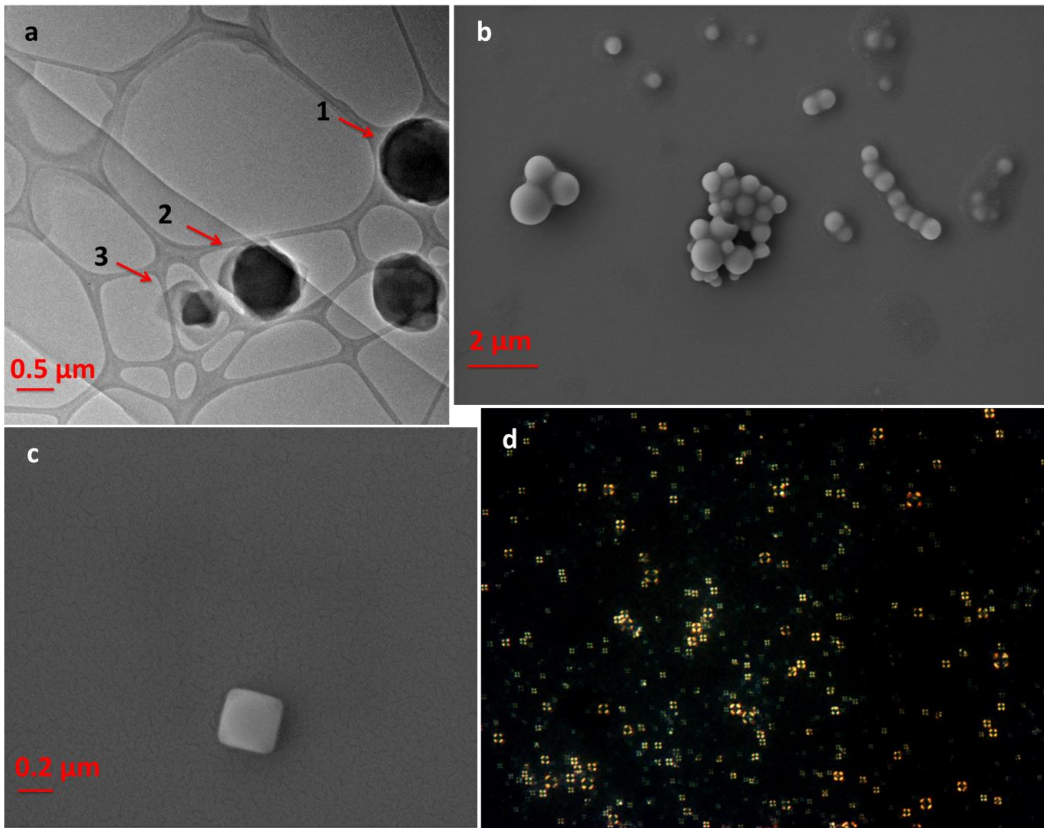


**Figure 5. (a) TEM of $CH_{pl}$ 1st intermediate presenting particles undergoing a transformation in three steps; (1) represents the initially formed liquid crystalline particles while (2) and (3) represent the transformation of those liquid crystalline particles to crystals via Ostwald ripening (b) SEM $CH_{sh}$ 1st intermediate (c) 2nd intermediate and (d) PLM 1st intermediate (magnification of 500).**

### 3.5. Computational investigations

Bravais, Friedel, Donnay and Harker (BFDH) simulations, a simplified representation of the thermodynamic shape, also known as "equilibrium" habit devoid of any interaction with the milieu, yielded ten unique facets along with their planes, % surface area and distance from the centre. The eight most morphologically important faces exhibiting the largest surface area are displayed in Table 2.

**Table 2. The eight most important faces bounding the crystal with their surface area and distance from the origin as measured for the BFDH morphology.**

| *hkl* | Relative face area (%) | Distance from the centre (Å) |
|---|---|---|
| $(\mathbf{001})$ | 17.45 | 20.16 |
| $(\mathbf{00\bar{1}})$ | 17.45 | 20.16 |
| $(\mathbf{010})$ | 15.0 | 19.00 |

| | | |
|---|---|---|
| $(\mathbf{0\bar{1}0})$ | 15.0 | 19.00 |
| $(\mathbf{011})$ | 7.7 | 16.35 |
| $(\mathbf{0\bar{1}\bar{1}})$ | 7.7 | 16.35 |
| $(\mathbf{100})$ | 5.2 | 8.47 |
| $(\mathbf{\bar{1}00})$ | 5.2 | 8.47 |

The BFDH model indicates that (001) and (010) are the most important faces since they constitute 17.45 and 15.0% of the external crystal surface, which further justify the use of $(00l)$ and $(0l0)$ diffractions to calculate the MD parameter earlier. For the different crystal habits, crystal slicing was carried out using Mercury 3.5.1 software based on the PRXRD data to investigate the exposed functional groups on the affected faces.

For the three habits, as demonstrated earlier, the intensities of PRXRD peaks at 4.6 and 13.9 2θ°, corresponding to the (010) and (030) planes, increased in the rank order: $CH_{tw} < CH_{pl} < CH_{sh}$. On the other hand, the intensity of the peak corresponding to (001) was the greatest for $CH_{tw}$, intermediate in $CH_{pl}$ and this peak was almost invisible in $CH_{sh}$. This observation is in agreement with the face indexing (Figure SI.6) and preferred orientation investigations for $CH_{tw}$, where the (010) face was identified as the largest flat surface in the investigated crystals. SCXRD analysis and face indexing was only performed for $CH_{tw}$, as it was not feasible in the case of $CH_{pl}$ and $CH_{sh}$ due to the crystals being very thin and too fragile to be handled. It is well known that during a crystallisation process, some facets will have a faster growing rate than others where the slow growing faces will have larger area in the final crystal. Therefore, additives or solvent molecules interacting with a specific facet will retard the growth of that facet and thus increase its relative area [44]. Thus the growth of the (010) face is expected to be retarded during the crystal growth process, while the growth of (001) face is promoted. Figure SI.7 illustrates the growth of both planes with the (010) face forming an angle of 73.175° with the (001) face which further supporting the above discussion [30]. An investigation of the exposed functional groups on the surface of both faces, as indicated in Figures SI.7 and 6a, revealed the abundance of polar functional groups including O17, O14, N9, N10, N12, N40C and N41C of each asymmetric unit on the (010) face. In contrast, nonpolar groups dominate the (001) face including C18, C19, C20, C21, C25, C26, C31 and the chlorine attached to the aromatic ring. The rule of thumb is that polar additives yield crystal habits with higher relative surface area of polar faces than nonpolar counterparts [45]. Kumar et al. observed a correlation between the polar:nonpolar proportional surface area of nifedipine crystals to the proportion of polar:nonpolar crystallising solvents [39]. It should be highlighted that nifedipine is capable of donating hydrogen atoms to form conventional H-bonds and thus can interact with polar aprotic solvents while, based

on the structural analysis carried out with Mercury 3.5.1, ITR cannot. This is further confirmed from the Hirshfeld surface analysis (Figure 6b) showing a limited number of red hot spots. The red spots correspond to $d_{norm}$ reciprocal interactions stronger than van der Waals interactions such as hydrogen bonds and/or weaker short-range contacts. The 2D fingerprint plot displays 'wing' like shapes (red arrows in Figure 6c) characteristic of the weak donor/weak acceptor type (C-H···π), while the absence of sharp features pointing to the left of the plot indicates the absence of any conventional strong H-bond donor/strong H-bond acceptor contacts [31].

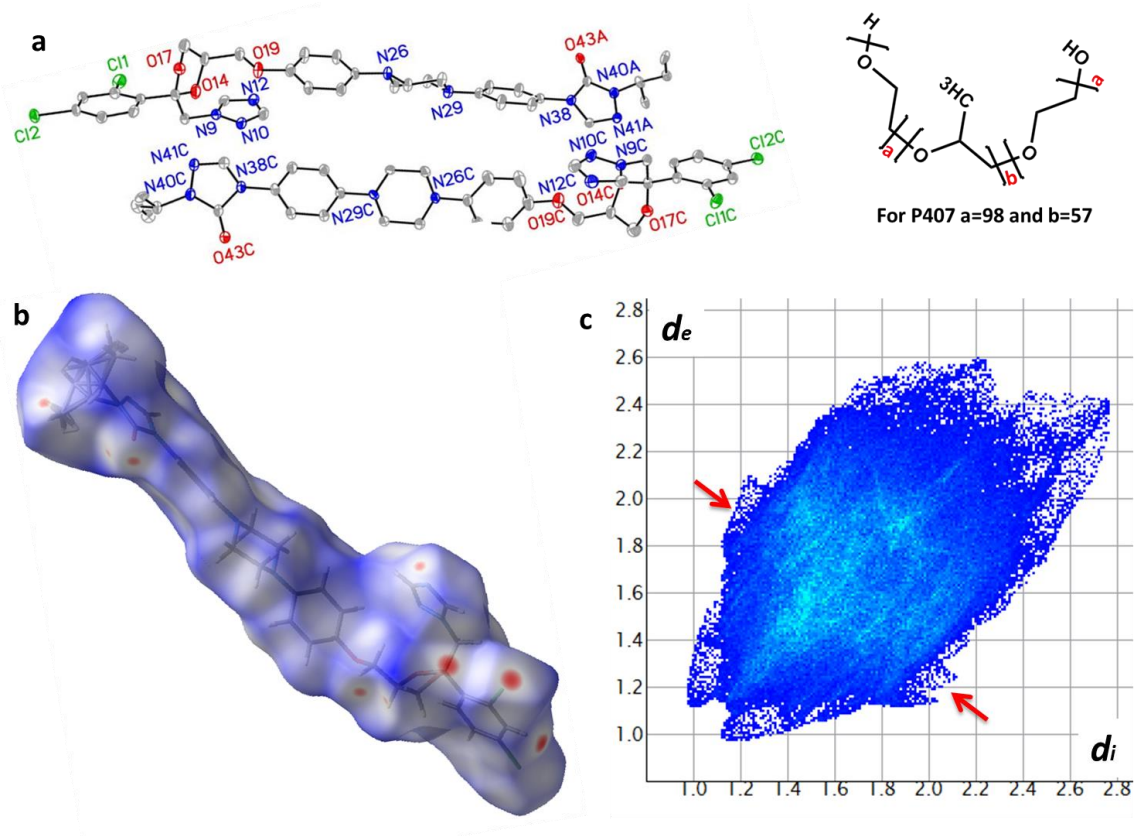


**Figure 6. (a) Asymmetric unit of ITR (hydrogen atoms omitted and only non-carbon atoms labelled for clarity) and a chemical structure of P407 (ChemDraw®), (b) Hirshfeld surface of ITR, shown in the transparent mode and (c) 2D fingerprint plot of ITR showing the "wing" like features (red arrows) characteristic of C-H···π reciprocal interactions.**

To understand the possible type of interactions on the faces of question, a full interaction map was generated for those facets using Mercury 3.5.1 as demonstrated in Figure 7 with opacity level applied. The highly opaque contours are indicative of greater chances of the investigated type of interaction at a certain grid point to occur [30]. The red hotspots, indicative of possible interactions with H-acceptors, observed in the surface mapping of both (010) and (001) faces are non-

conventional hydrogen bonding donors due to the weak donor type (C-H···acceptor) interactions. ITR molecule can serve as a conventional H-bond acceptor only, thus it can interact, through H-bonds, with protic solvents only. The (010) plane shows more preferred interaction sites for H-bond donors than the (001) plane. Therefore, herein, in the case of a mixture of acetone (aprotic) and water (protic), water is expected to interact with the polar surfaces and inhibit their growth thus the correlation of protic:aprotic crystallising solvent proportion to the polar:nonpolar crystal surface area, could be applicable. Poloxamer has the ability to form hydrogen bonds as it is an H-bond donor and an H-bond acceptor, thus it may react with the (010) facet. The effect of P407 was clear in the contour map (Figure 3) as $CH_{pl}$ and $CH_{sh}$ were only observable upon the inclusion of P407 in the solvent phase.

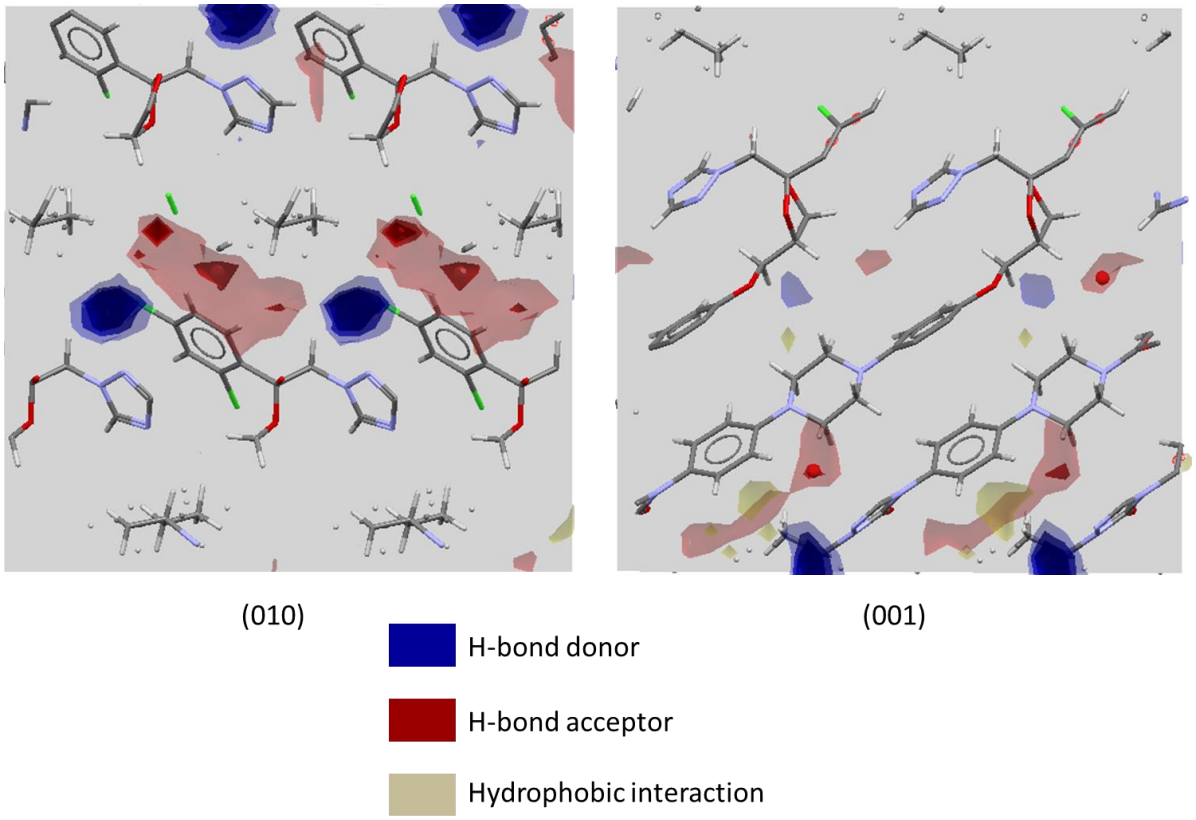


**Figure 7. Packing diagram and interaction maps of (010) and (001) surfaces illustrating the possible hydrogen bond donor, hydrogen bond acceptor and hydrophobic interactions of functional groups on each surface. The higher the opacity of the contour, the greater the chance of the investigated interaction to take place.**

### 3.6. Impact of crystal habit on the wetting and water sorption behaviour of ITR

The advancing contact angle using deionised water reflected the wettability properties of the crystals. The starting material of "as received" ITR had the highest contact angle with the water droplets (123±2°) indicating high hydrophobicity of the exposed surface. The measured contact

angle was lower for $CH_{tw}$ (113±3°) followed by $CH_{pl}$ (58±4°). $CH_{sh}$ had the lowest angle of 48±2° indicating the least hydrophobic surface (Figure SI.8).

DVS was used to more fully investigate the effect of different habits on the interaction with water molecules. The correlation between the surface polarity and its ability to adsorb water has been demonstrated before for materials such as carbon nanotubes [46]. Nevertheless, the influence of surface polarity, due to the crystal habit manipulation, on water adsorption/absorption properties is not studied often. Therefore, it was of a great interest to investigate this effect especially that it has a direct impact on dissolution behaviour and physical stability [47]. When we only consider the total amount of sorbed water (Figure SI.9), there was no difference between the behaviour of the three different habits. Therefore, there was a need to establish a quantitative correlation between the distribution of water in the different systems and the % RH via fitting the DVS data with the Young and Nelson model (Eqs. 2 and 3). Using this model, the difference in water distribution within the three systems was demonstrated (Figure 8). In general, the model showed a good fitting for all crystal habits as inferred from the R-sq values.

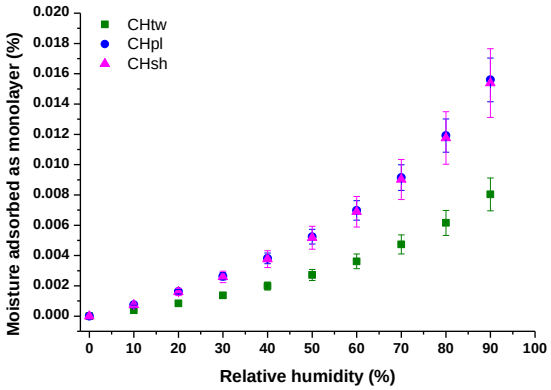


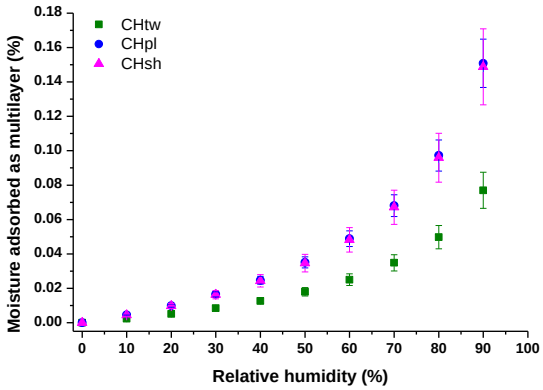


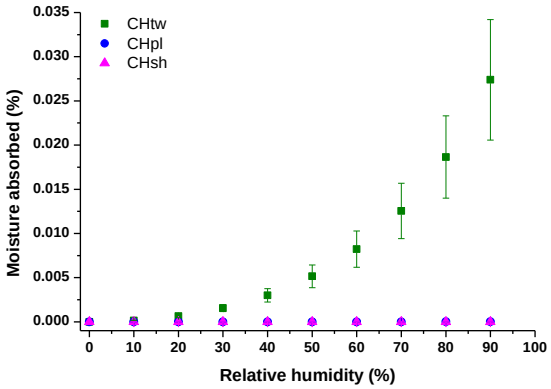


| Sample | R-sq | E | A | B |
|---|---|---|---|---|
| CHtw | 0.929 | 2.91 ± 0.008 | 1.06E-4 ± 1E-05 | 4.02E-4 ± 9E-05 |
| CHpl | 0.983 | 2.94 ± 0.003 | 2.07E-4 ± 1E-05 | 1.31E-7 ± 1E-07 |
| CHsh | 0.931 | 2.94 ± 0.004 | 2.04E-4 ± 3E-05 | 9.47E-9 ± 1E-08 |

**Figure 8. Moisture distribution for the three different habits as (a) adsorbed monolayer, (b) adsorbed multilayer and (c) internally absorbed and a summary table of the estimated parameters E, A and B based on the Young and Nelson model and fit correlation coefficients for all samples.**

The amount of water adsorbed, as mono and multilayer, on the surface of $CH_{pl}$ and $CH_{sh}$ crystals was comparable and it was about twice that adsorbed on $CH_{tw}$ crystals as shown in Figure 8a and b. This can be confirmed by the values of $A$ parameter, which was comparable for $CH_{pl}$ and $CH_{sh}$ and was twice that of $CH_{tw}$. These findings are consistent with the wettability results and further indicate that more hydrophilic groups are exposed on the surfaces of $CH_{pl}$ and $CH_{sh}$ than on the $CH_{tw}$ surfaces. The comparable moisture adsorption isotherms for $Ch_{pl}$ and $CH_{sh}$, even though $CH_{sh}$ showed a slightly better wettability value, can be due to the fragility of $Ch_{sh}$ (Figure SI.10) crystals, which can lead to the exposure of other hydrophobic faces upon breakage. However, in the contact angle measurements only the wettability of (010) face is preferentially probed due to the preferred orientation effect. In contrast, the $CH_{tw}$ sample absorbed statistically significantly ($p \leq 0.05$) more water (0.027±0.006%) and exhibited a higher B parameter than the $CH_{pl}$ and $CH_{sh}$ samples, which practically did not absorb any moisture. Although the amount absorbed was very small, it was a surprising behaviour by otherwise highly hydrophobic ITR crystals. This minute water absorption could possibly be attributed to the presence of crystal packing defects due to the twinning boundary which could allow some water diffusion above 40% RH. In a perfectly packed crystal, based on Mercury 3.5.1 calculations [48], ITR possesses lattice voids (Figure SI.11), which can fit a molecule with a maximum radius of approximately 1.16 Å. This value is smaller than the radius of a water molecule (1.5 Å) [49]. In other words, there is no space available for a single water molecule in a defect-free crystal. The presence of some internally absorbed water can also be inferred from the hysteresis observed for $CH_{tw}$ (Figure SI.8), where more water is being held during the desorption cycle than during sorption [24, 50]. PRXRD investigations of the three crystal habits following a full DVS cycle (sorption and desorption) (Figure SI.12) revealed that they are physically stable under the investigated conditions.

**4. Conclusions**

Itraconazole has been shown to form three distinct crystal habits/intergrowths when crystallised from a mixture of protic/aprotic solvents, in the presence of P407, due to the isotropic chemical functionalities on crystal facets which interact differently with components of the crystallisation mixture. A liquid-liquid crystalline phase separation was observed preceding the crystal growth phase. The shape of the final crystals is governed by the protic/aprotic solvent ratio, polymer concentration and crystallisation temperature. The twinned blade-like $CH_{tw}$ crystals exhibited highly hydrophobic surfaces and showed considerable permeability to water vapour due to the presence of twin boundary stacking defects. The $CH_{pl}$ and $CH_{sh}$ samples displayed comparable water adsorption/absorption behaviour. These two habits were practically unable to absorb water

although their surface can adsorb twice the amount of water molecules than $CH_{tw}$, which could be ascribed to the large 010 crystal facet surface area with the abundance of hydrophilic functionalities. This study expands investigations of the impact of crystal habit manipulation on API's physicochemical properties beyond the well-known and established solubility improvement approaches, extensively studied in the literature.

**Associated content**

**Supporting Information**

The Supporting Information file contains a simulated X-ray diffraction pattern for ITR, PTXRD, DSC thermograms, real time imaging of the crystallisation process, face indexing of $CH_{tw}$, crystal packing, contact angle measurements, DVS total sorption isotherms and additional SEM data.

**Acknowledgements**

This work was funded by the Libyan Ministry of Higher Education and Scientific Research and the Science Foundation Ireland under Grant No. 12/RC/2275 (Synthesis and Solid State Pharmaceuticals Centre). The authors would like to thank Dr. Grzegorz Garbacz (Physiolution GmbH, Germany) for kindly supplying ITR, Prof. Marian Paluch, Dr. Zaneta Wojnarowska and Ms. Karolina Jurkiewicz (Institute of Physics, University of Silesia, Katowice, Poland) for PTXRD data, Dr. Brendan Twamley (School of Chemistry, TCD) for performing SCXRD and Mr. Peter O'Connell (School of Pharmacy and Pharmaceutical Sciences, TCD) for providing access to the contact angle analyser.

**References**


1. Stoica, C.; Verwer, P.; Meekes, H.; van Hoof, P. J. C. M.; Kaspersen, F. M.; Vlieg, E. Understanding the effect of a solvent on the crystal habit. *Cryst Growth Des* **2004,** *4*, (4), 765-768.

2. Nagy, Z. K.; Fujiwara, M.; Braatz, R. D. Modelling and control of combined cooling and antisolvent crystallization processes. *J Process Contr* **2008,** *18*, (9), 856-864.

3. Shahidzadeh-Bonn, N.; Rafai, S.; Bonn, D.; Wegdam, G. Salt crystallization during evaporation: Impact of interfacial properties. *Langmuir* **2008,** *24*, (16), 8599-8605.

4. Hancock, B. C.; Parks, M. What is the true solubility advantage for amorphous pharmaceuticals? *Pharm Res* **2000,** *17*, (4), 397-404.

5. Haleblian, J. K. Characterization of Habits and Crystalline Modification of Solids and Their Pharmaceutical Applications. *J Pharm Sci* **1975,** *64*, (8), 1269-1288.

6. Shell, J. W. X-Ray and Crystallographic Applications in Pharmaceutical Research .3. Crystal Habit Quantitation. *J Pharm Sci* **1963,** *52*, (1), 100-&.

7. Hartman, P.; Bennema, P. The Attachment Energy as a Habit Controlling Factor .1. Theoretical Considerations. *J Cryst Growth* **1980,** *49*, (1), 145-156.

8. Modi, S. R.; Dantuluri, A. K. R.; Puri, V.; Pawar, Y. B.; Nandekar, P.; Sangamwar, A. T.; Perumalla, S. R.; Sun, C. C.; Bansal, A. K. Impact of Crystal Habit on Biopharmaceutical Performance of Celecoxib. *Cryst Growth Des* **2013,** *13*, (7), 2824-2832.

9. Tenho, M.; Heinanen, P.; Tanninen, V. P.; Lehto, V. P. Does the preferred orientation of crystallites in tablets affect the intrinsic dissolution? *J Pharm Biomed Anal* **2007,** *43*, (4), 1315-23.

10. Modi, S. R.; Dantuluri, A. K. R.; Perumalla, S. R.; Sun, C. Q. C.; Bansal, A. K. Effect of Crystal Habit on Intrinsic Dissolution Behavior of Celecoxib Due to Differential Wettability. *Cryst Growth Des* **2014,** *14*, (10), 5283-5292.

11. Purkayastha, A.; Yan, Q. Y.; Raghuveer, M. S.; Gandhi, D. D.; Li, H. F.; Liu, Z. W.; Ramanujan, R. V.; Borca-Tasciuc, T.; Ramanath, G. Surfactant-directed synthesis of branched bismuth telluride/sulfide core/shell nanorods. *Adv Mater* **2008,** *20*, (14), 2679-+.

12. Sunagawa, I., *Crystals; Growth, Morphology and Perfection*. Cambridge University Press: Cambridge, 2005.

13. Jocelyn, J.; Pidgeon, R. T. Examples of Twinning and Parallel Growth in Zircons from Some Precambrian Granites and Gneisses. *Mineral Mag* **1974,** *39*, (305), 587-594.

14. Borodi, G.; Pop, M. M.; Onija, O.; Filip, X. Distinct Disordered Forms of Promethazine Hydrochloride: A Case of lntergrowth of Polymorphic Domains? *Cryst Growth Des* **2012,** *12*, (12), 5846-5851.

15. Mishra, M. K.; Desiraju, G. R.; Ramamurty, U.; Bond, A. D. Studying Microstructure in Molecular Crystals With Nanoindentation: Intergrowth Polymorphism in Felodipine. *Angew Chem Int Edit* **2014,** *53*, (48), 13102-13105.

16. Yin, Y. N.; Chow, P. S.; Tan, R. B. H. Molecular Simulation Study of the Effect of Various Additives on Salbutamol Sulfate Crystal Habit. *Mol Pharm* **2011,** *8*, (5), 1910-1918.

17. Wood, W. M. L. A bad (crystal) habit - and how it was overcome. *Powder Technol* **2001,** *121*, (1), 53-59.

18. Weissbuch, I.; Lahav, M.; Leiserowitz, L. Toward stereochentical control, monitoring, and understanding of crystal nucleation. *Cryst Growth Des* **2003,** *3*, (2), 125-150.

19. Tian, F.; Baldursdottir, S.; Rantanen, J. Effects of Polymer Additives on the Crystallization of Hydrates: A Molecular-Level Modulation. *Mol Pharm* **2009,** *6*, (1), 202-210.

20. Tiller, W. A. Dendrites - Understanding of Familiar Phenomenon Has Led to Development of Useful Man-Made Materials. *Science* **1964,** *146*, (364), 871-&.

21. Odds, F. C.; Oris, M.; Van Dorsselaer, P.; Van Gerven, F. Activities of an intravenous formulation of itraconazole in experimental disseminated Aspergillus, Candida, and Cryptococcus infections. *Antimicrob agents ch* **2000,** *44*, (11), 3180-3183.

22. Peeters, O. M.; Blaton, N. M.; DeRanter, C. J. cis-2-sec-butyl-4-{4-[4-(4-{[2-(2,4-dichlorophenyl)-2-(1H-1,2,4-triazol-1-ylmethyl)-1,3-dioxolan-4-yl]methoxy}phenyl)-1-piperazinyl]phenyl}-2,4-dihydro-3H-1,2,4-triazol-3-one (itraconazole). *Acta Crystallogr C* **1996,** *52*, 2225-2229.

23. Werling, J., Doty, M.J., Rebbeck, C.L., Wong, J.C.T., Kipp, J.E., Polymorphic Form of Itraconazole. **2007**. U.S Patents: 7193084

24. Mugheirbi, N. A.; Paluch, K. J.; Tajber, L. Heat induced evaporative antisolvent nanoprecipitation (HIEAN) of itraconazole. *Int J Pharm* **2014,** *471*, (1-2), 400-411.

25. Rohrs, B. R.; Thamann, T. J.; Gao, P.; Stelzer, D. J.; Bergren, M. S.; Chao, R. S. Tablet dissolution affected by a moisture mediated solid-state interaction between drug and disintegrant. *Pharm Res* **1999,** *16*, (12), 1850-1856.

26. Puncochova, K.; Heng, J. Y. Y.; Beranek, J.; Stepanek, F. Investigation of drug-polymer interaction in solid dispersions by vapour sorption methods. *Int J Pharm* **2014,** *469*, (1), 159-167.

27. Zolotoyabko, E. Determination of the degree of preferred orientation within the March-Dollase approach. *J Appl Crystallogr* **2009,** *42*, 513-518.

28. Grzybowska, K.; Paluch, M.; Grzybowski, A.; Wojnarowska, Z.; Hawelek, L.; Kolodziejczyk, K.; Ngai, K. L. Molecular Dynamics and Physical Stability of Amorphous Anti-Inflammatory Drug: Celecoxib. *J Phys Chem B* **2010,** *114*, (40), 12792-12801.

29. Verdonk, M. L.; Cole, J. C.; Watson, P.; Gillet, V.; Willett, P. SuperStar: Improved knowledge-based interaction fields for protein binding sites. *J Mol Biol* **2001,** *307*, (3), 841-859.

30. Wood, P. A.; Olsson, T. S. G.; Cole, J. C.; Cottrell, S. J.; Feeder, N.; Galek, P. T. A.; Groom, C. R.; Pidcock, E. Evaluation of molecular crystal structures using Full Interaction Maps. *Crystengcomm* **2013,** *15*, (1), 65-72.

31. Spackman, M. A.; McKinnon, J. J. Fingerprinting intermolecular interactions in molecular crystals. *Crystengcomm* **2002,** *4*, 378-392.

32. He, X. R.; Barone, M. R.; Marsac, P. J.; Sperry, D. C. Development of a rapidly dispersing tablet of a poorly wettable compound - formulation DOE and mechanistic study of effect of formulation excipients on wetting of celecoxib. *Int J Pharm* **2008,** *353*, (1-2), 176-186.

33. Overhoff, K. A.; Engstrom, J. D.; Chen, B.; Scherzer, B. D.; Milner, T. E.; Johnston, K. P.; Williams, R. O. Novel ultra-rapid freezing particle engineering process for enhancement of dissolution rates of poorly water-soluble drugs. *Eur J Pharm Biopharm* **2007,** *65*, (1), 57-67.

34. Schonberg, J. A.; Dasgupta, S.; Wayner, P. C. An Augmented Young-Laplace Model of an Evaporating Meniscus in a Microchannel with High Heat-Flux. *Exp Therm Fluid Sci* **1995,** *10*, (2), 163-170.

35. Bravo-Osuna, I.; Ferrero, C.; Jimenez-Castellanos, M. R. Water sorption-desorption behaviour of methyl methacrylate-starch copolymers: effect of hydrophobic graft and drying method. *Eur J Pharm Biopharm* **2005,** *59*, (3), 537-548.

36. Lofgren, G. Experimental Study of Plagioclase Crystal Morphology - Isothermal Crystallization. *Am J Sci* **1974,** *274*, (3), 243-273.

37. Heising, J.; Kanatzidis, M. G. Exfoliated and restacked MoS2 and WS2: Ionic or neutral species? Encapsulation and ordering of hard electropositive cations. *J Am Chem Soc* **1999,** *121*, (50), 11720-11732.

38. Tenho, M.; Aaltonen, J.; Heinanen, P.; Peltonen, L.; Lehto, V. P. Effect of texture on the intrinsic dissolution behaviour of acetylsalicylic acid and tolbutamide compacts. *J Appl Crystallogr* **2007,** *40*, 857-864.

39. Kumar, D.; Shastri, N. R. Designed Isomorphism of Nifedipine: A Joint Experimental and Molecular Simulation Study with Screened Solvents and Antisolvents. *Cryst Growth Des* **2014,** *14*, (1), 326-338.

40. Gharbi, M. A.; Cavallaro, M.; Wu, G. X.; Beller, D. A.; Kamien, R. D.; Yang, S.; Stebe, K. J. Microbullet assembly: interactions of oriented dipoles in confined nematic liquid crystal. *Liq Cryst* **2013,** *40*, (12), 1619-1627.

41. Mugheirbi, N. A., Tajber, L. Mesophase and size manipulation of itraconazole liquid crystalline nanoparticles produced via quasi nanoemulsion precipitation. *Eur J Pharm Biopharm* **2015,** 10.1016/j.ejpb.2015.08.005.

42. Ilevbare, G. A.; Taylor, L. S. Liquid-Liquid Phase Separation in Highly Supersaturated Aqueous Solutions of Poorly Water-Soluble Drugs: Implications for Solubility Enhancing Formulations. *Cryst Growth Des* **2013,** *13*, (4), 1497-1509.

43. Mosquera-Giraldo, L. I.; Taylor, L. S. Glass-Liquid Phase Separation in Highly Supersaturated Aqueous Solutions of Telaprevir. *Mol Pharm* **2015,** *12*, (2), 496-503.

44. Addadi, L.; Berkovitchyellin, Z.; Weissbuch, I.; Vanmil, J.; Shimon, L. J. W.; Lahav, M.; Leiserowitz, L. Growth and Dissolution of Organic-Crystals with Tailor-Made Inhibitors - Implications in Stereochemistry and Materials Science. *Angew Chem Int Edit* **1985,** *24*, (6), 466-485.

45. Myerson, A., *Handbook of Industrial Crystallization*. 2 ed.; Butterworth-Heinemann: Woburn, 2002.

46. Bradley, R. H.; Andreu, A.; Cassity, K.; Osbeck, S.; Andrews, R.; Meier, M.; Johnston, C. Dependence of Water Vapour Adsorption on the Polarity of the Graphene Surfaces of Multi-wall Carbon Nanotubes. *Adsorpt Sci Technol* **2010,** *28*, (10), 903-912.

47. Puri, V.; Dantuluri, A. K.; Kumar, M.; Karar, N.; Bansal, A. K. Wettability and surface chemistry of crystalline and amorphous forms of a poorly water soluble drug. *Eur J Pharm Sci* **2010,** *40*, (2), 84-93.

48. Barbour, L. J. Crystal porosity and the burden of proof. *Chem comm* **2006**, (11), 1163-1168.

49. Hermann, R. B. Theory of Hydrophobic Bonding .II. Correlation of Hydrocarbon Solubility in Water with Solvent Cavity Surface Area. *J Phys Chem* **1972,** *76*, (19), 2754-2759.

50. York, P. Analysis of Moisture Sorption Hysteresis in Hard Gelatin Capsules, Maize Starch, and Maize Starch - Drug Powder Mixtures. *J Pharm Pharmacol* **1981,** *33*, (5), 269-273.